Atmospheric
Chemistry
and Physics

Supplement of

Contribution of local and remote anthropogenic aerosols to a record-breaking torrential rainfall event in Guangdong Province, China

Zhen Liu et al.

Correspondence to: Steve Hung Lam Yim (steveyim@cuhk.edu.hk)

S1. WRF-Chem model configuration

WRF-Chem is a fully online model coupled with gas-phase chemistry mechanisms and aerosol physiochemical modules. In this model, chemical and meteorological components share the same grid coordinates, time steps, transport schemes, and subgrid physics. The meteorological component (WRF) of this coupled model uses an Eulerian dynamical core with a nonhydrostatic solver (Skamarock et al., 2008). Gas-phase chemical reactions are estimated using the carbon bond chemical mechanism (Zaveri and Peters, 1999). Aerosol physics and chemistry are treated using the Model for Simulating Aerosol Interactions and Chemistry (MOSAIC) scheme (Zaveri et al., 2008) with aqueous chemistry. The aerosol size distribution is represented by four discrete size bins within the MOSAIC scheme: 0.039–0.156 μm, 0.156–0.625 μm, 0.625–2.5 μm, and 2.5–10 μm (Fast et al., 2006). The approach to aerosol dry deposition is based on Binkowski and Shankar (1995). In-cloud (rainout) and below-cloud (washout) removal of aerosols by resolved clouds and precipitation are simulated following Easter et al. (2004) and Chapman et al. (2009), respectively. The transport and wet removal of aerosols by convective clouds are also considered using the Kain–Fritsch (KF) scheme (Kain and Fritsch, 1990) following Zhao et al. (2009, 2013). The major physical schemes of meteorological components comprise the KF cumulus scheme; the Yonsei University (YSU) planetary boundary layer (PBL) scheme (Hong et al., 2006); the National Center for Environmental Prediction, Oregon State University, Air Force, and Hydrologic Research Lab's (NOAH) land surface model (Chen and Dudhia, 2001); the Morrison two-moment scheme for cloud microphysics (Morrison et al., 2009); and the rapid radiative transfer for global (RRTMG) for both longwave and shortwave radiation schemes (Iacono et al., 2008). Aerosol interactions with shortwave and longwave radiation are incorporated into the model by linking aerosol optical properties, including optical depth, single-scattering albedo, and asymmetry factor, to RRTMG shortwave and longwave schemes, respectively (Zhao et al., 2010, 2011). The effects of ACI are estimated by considering the activation of aerosols to form cloud droplets based on the maximum supersaturation in the Morrison microphysical scheme (Chapman et al., 2009; Yang et al., 2011).

(a) Terrain Height
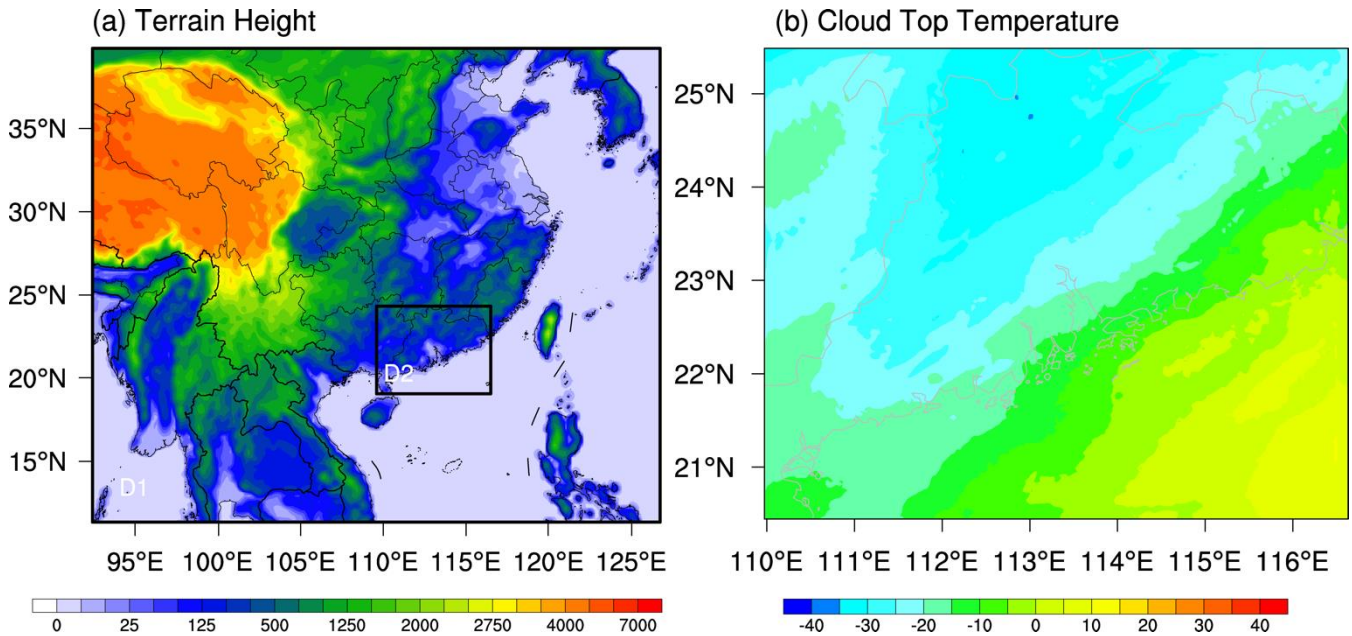
(b) Cloud Top Temperature

Figure S1. (a) WRF-Chem model two-nested domains with resolutions of 20 km and 4 km for domain 1 (D1) and domain 2 (D2), respectively. Shading represents terrain height (m). (b) Spatial distribution of 3-day averaged cloud top temperature (shading; °C) during December 14–16, 2013 over domain 2 in control run.
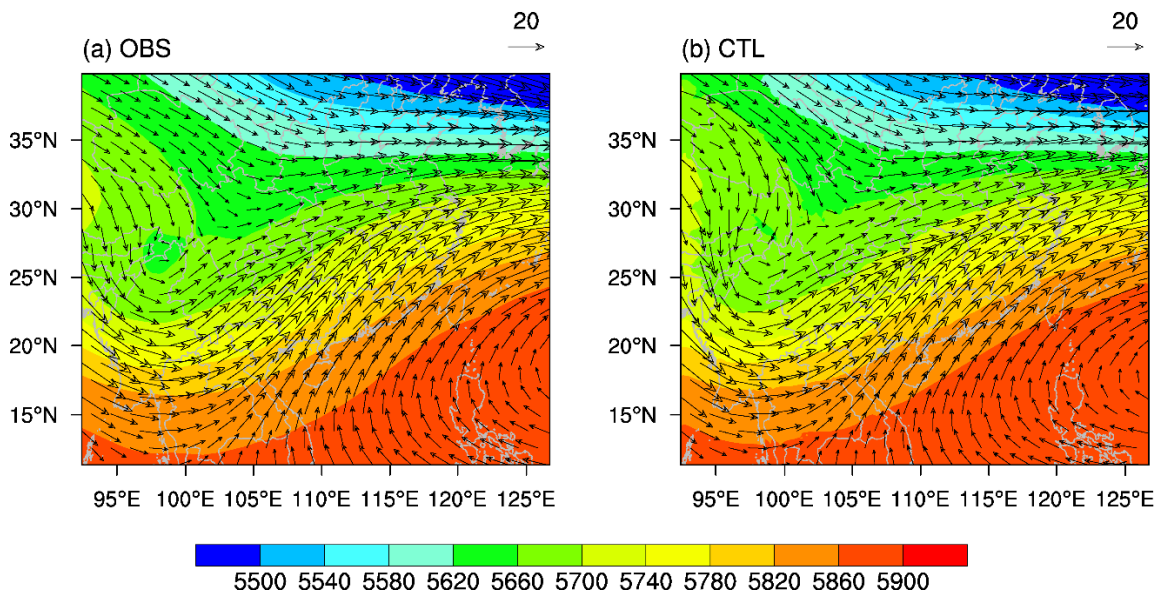
500-hPa Z and Wind

(a) OBS

(b) CTL

Figure S2. Spatial distribution of 3-day averaged 500-hPa wind (vector; m s⁻¹) and height (shading; m) during December 14–16, 2013 for (a) OBS from ERA-interim and (b) CTL from control simulation.
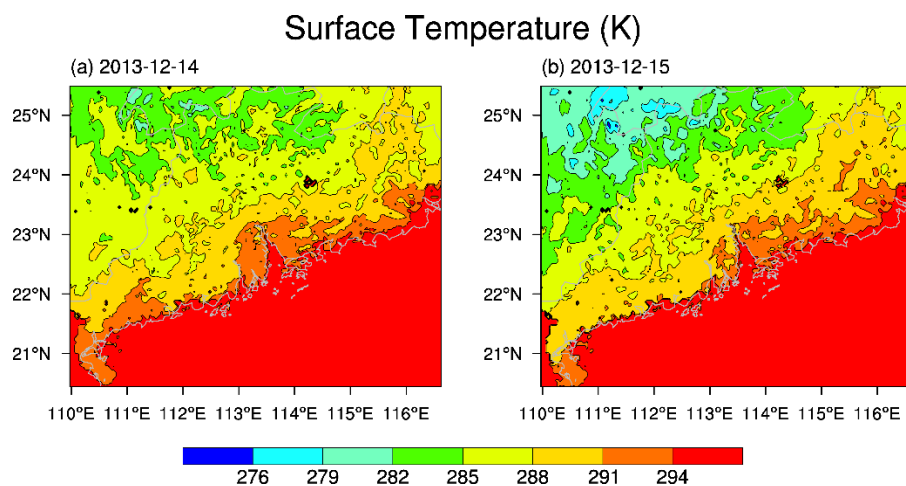

Figure S3. Spatial distribution of surface temperature (K) on (a) December 14 and (b) December 15 in 2013 in the CTL run.
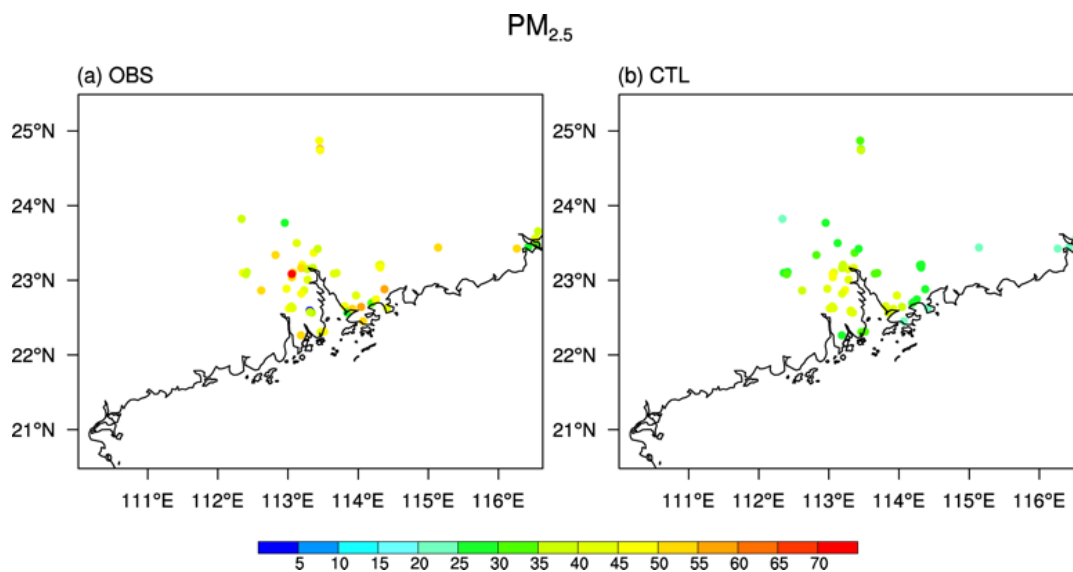

Figure S4. PM$_{2.5}$ concentration (μg m⁻³) average during December 14–16, 2013 for (a) observation and (b) control simulation. Colored circles denote in situ station locations.
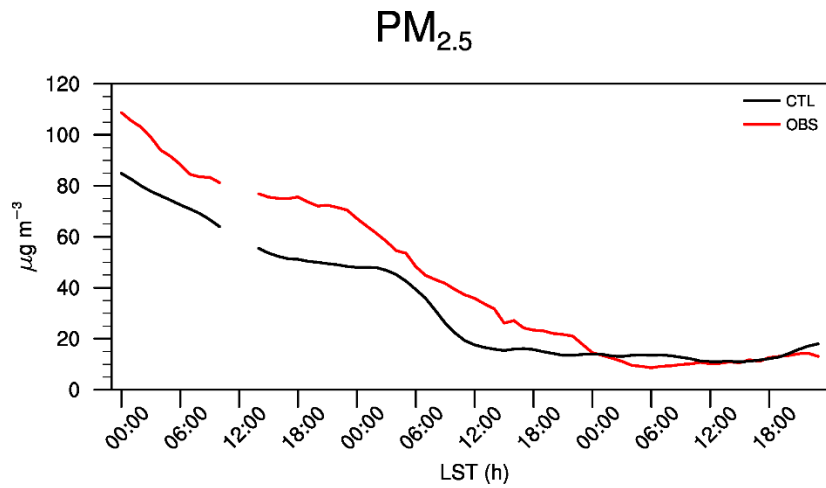
PM$_{2.5}$

Figure S5. Time series of PM$_{2.5}$ concentration averaged over all the air quality stations during December 14–16, 2013 for CTL (black) and OBS (red).
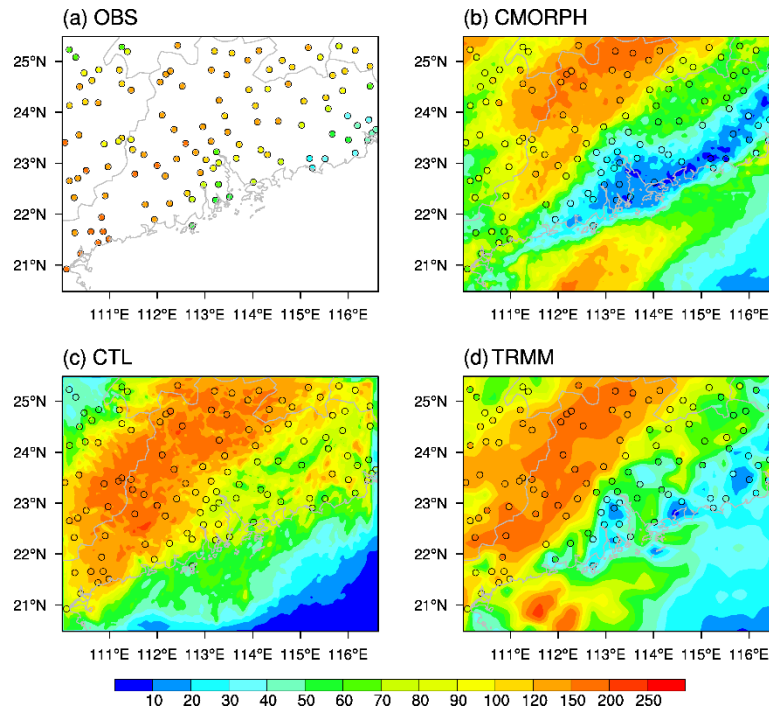

Figure S6. Spatial distribution of accumulated precipitation (mm) from 00Z on December 14, 2013 to 00Z on December 17, 2013 from (a) station observations (OBS), (b) CMORPH, (c) control simulation (CTL), and (d) TRMM. Circles denote locations of in situ observations.
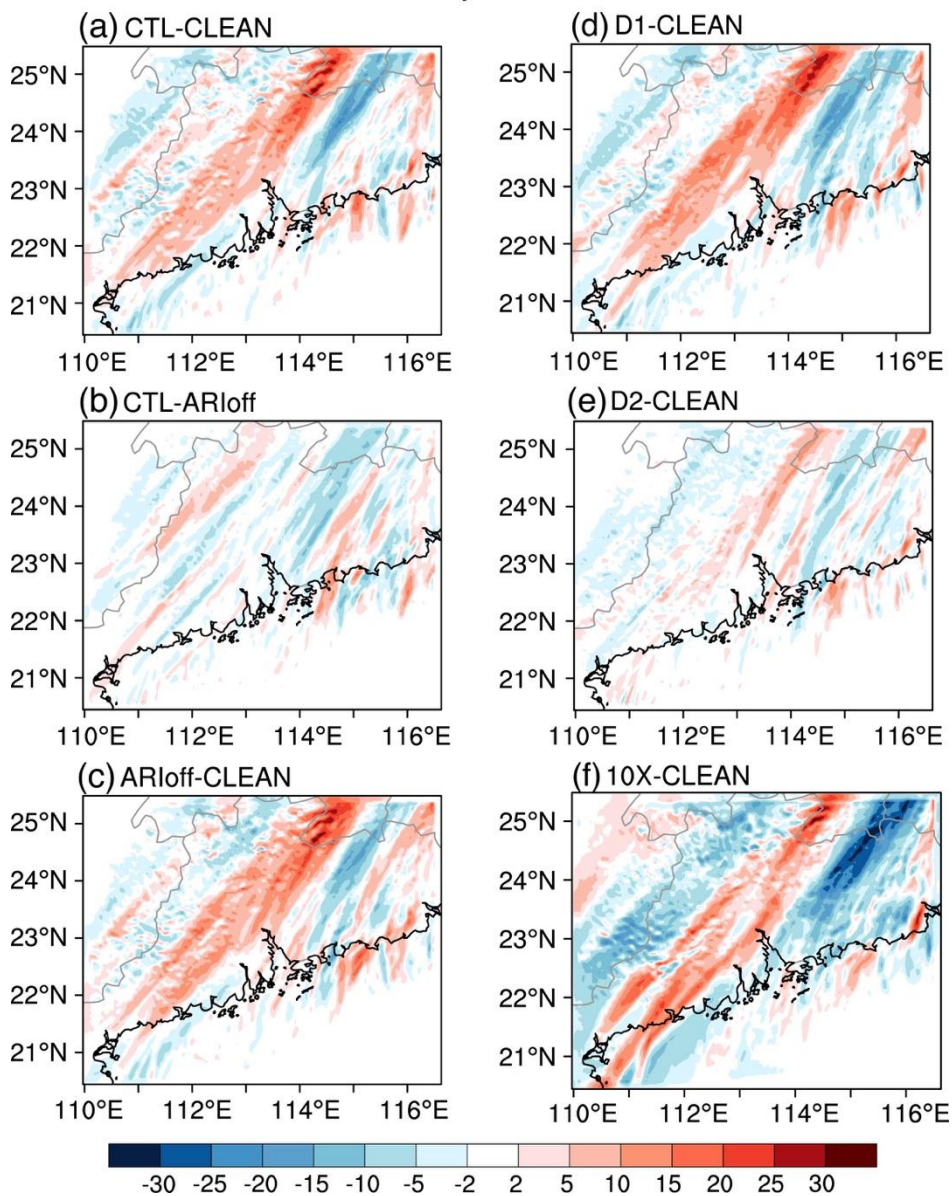
4

Precipitation

Figure S7. Differences in accumulated precipitation (mm) on December 16 between (a) CTL and CLEAN, (b) CTL and ARIoff, (c) ARIoff and CLEAN, (d) D1 and CLEAN, (e) D2 and CLEAN, and (f) 10× and CLEAN. ARIoff run refers to simulation with aerosol-radiation interactions off.
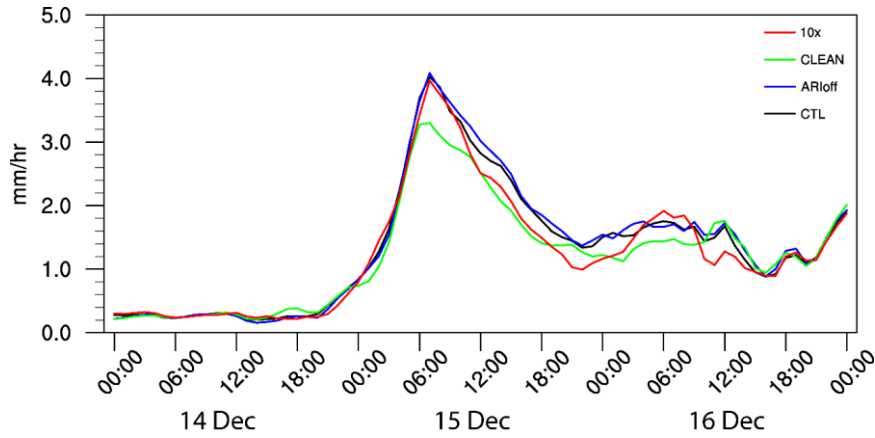
Figure S8. Time series of rain rate (mm h^{-1}) averaged over R1 (a) for 10× (red), CTL (black), ARIoff (blue), and CLEAN (green).
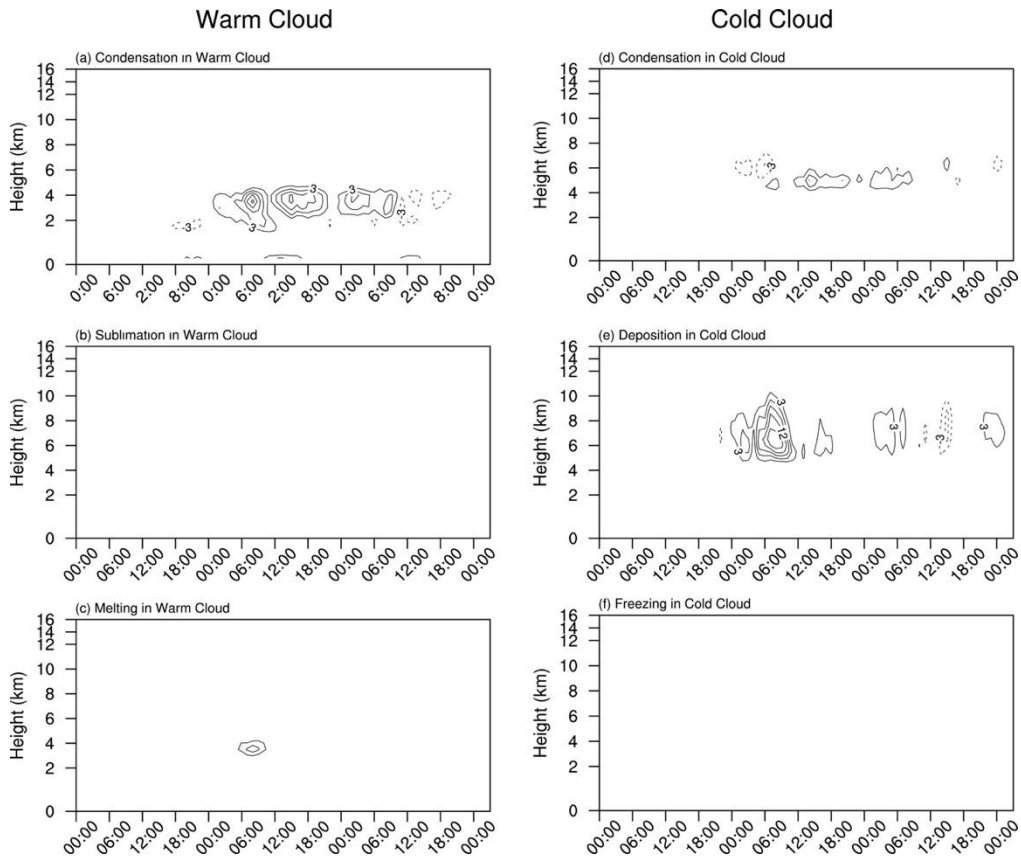

Figure S9. Differences with time (abscissa) and height (ordinate) in latent heat release (K d^{-1}) from (a) condensation, (b) deposition, and (c) freezing processes between CTL and CLEAN averaged over R1 for warm cloud. (d–f) Same as (a–c) but for cold cloud. Zero-value contour lines are omitted, and negative values are dashed. The contour interval is 3 K d^{-1}.
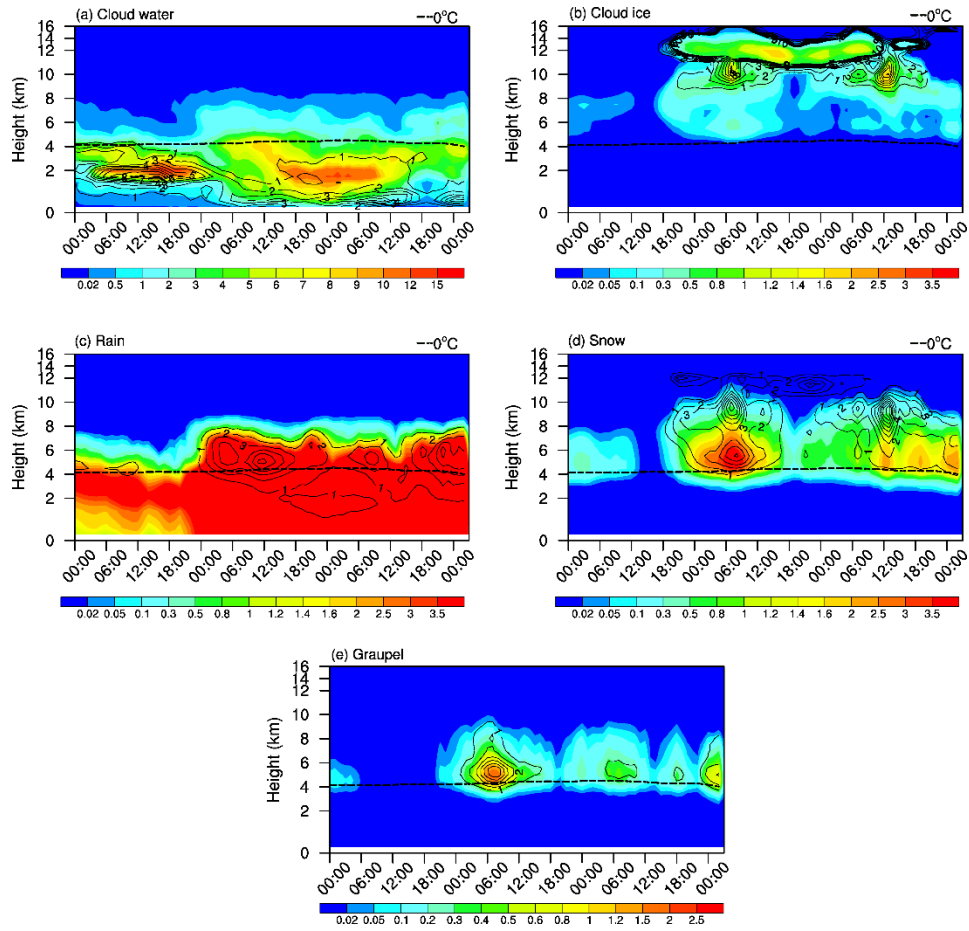
Figure S10. Distribution with time (abscissa) and height (ordinate) in (a) cloud water (shading; 10^{-5} kg kg^{-1}) and CDNC (contour; 10^{7} kg^{-1}), (b) cloud ice (shading; 10^{-5} kg kg^{-1}) and CINC (contour; 10^{4} kg^{-1}), (c) rain (shading; 10^{-5} kg kg^{-1}) and rain number concentration (contour; 10^{5} kg^{-1}), (d) snow (shading; 10^{-4} kg kg^{-1}) and snow number concentrations (contour; 10^{3} kg^{-1}), and (e) graupel (shading; 10^{-4} kg kg^{-1}) and graupel number concentration (contour; 10^{3} kg^{-1}) averaged over R1 in CTL run.
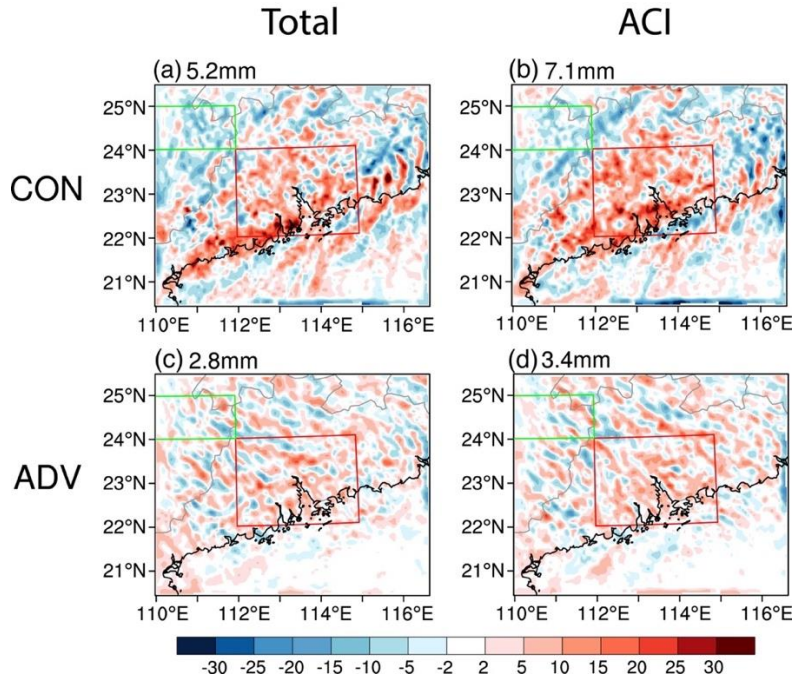
Figure S11. Differences in column-integrated moisture convergence (CON; mm) between (a) CTL and CLEAN and (b) ARIoff and CLEAN on December 15. (c, d) Same as (a, b) but for column-integrated advection of water vapor (ADV; mm). The numbers at the top-left corner of each panel represent the values averaged over R1.
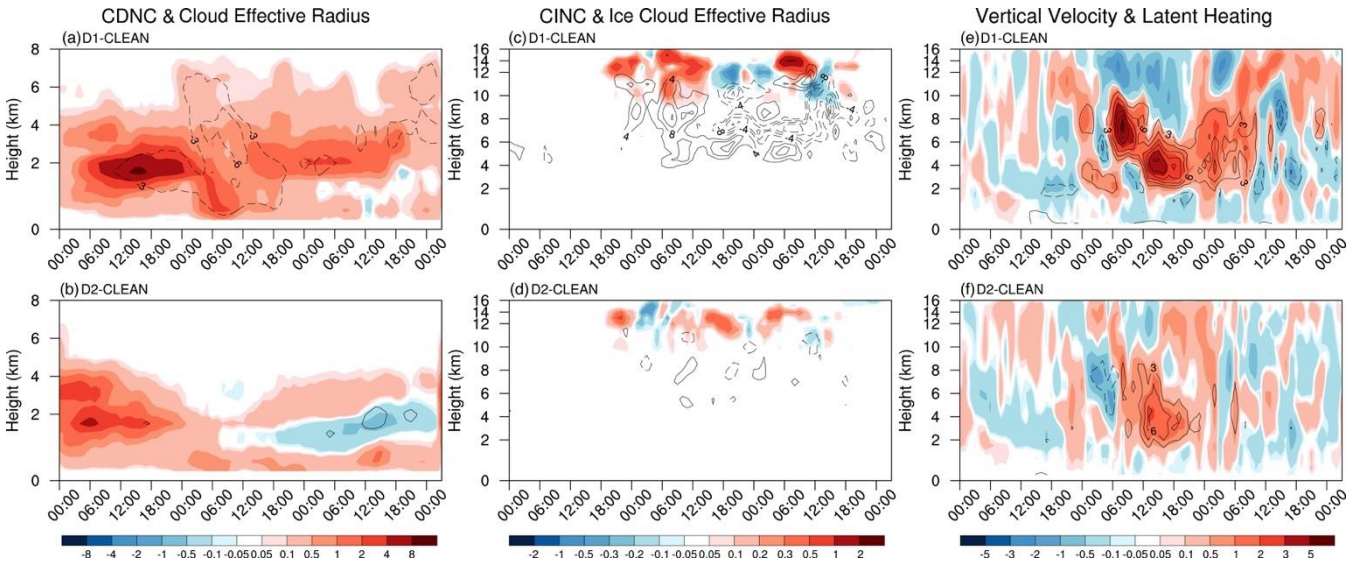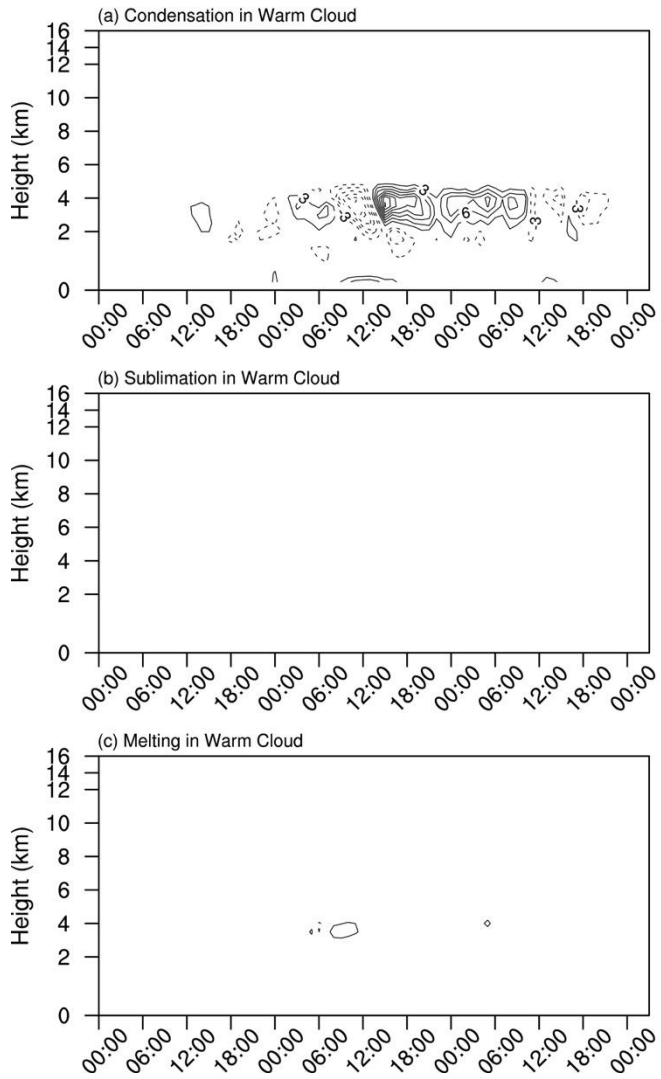

Figure S12. Differences with time (abscissa) and height (ordinate) in (a) CDNC (shading; 10^7 kg^{-1}) and cloud effective radius (contour; μm), (c) CINC (shading; 10^5 kg^{-1}) and ice cloud effective radius (contour; μm), and (e) vertical velocity (shading; cm s^{-1}) and latent heating (contour; K d^{-1}) averaged over R1 between D1 and CLEAN. (b, d, f) same as (a, c, e) but for differences between D2 and CLEAN. Zero-value contour lines are omitted, and negative values are dashed.
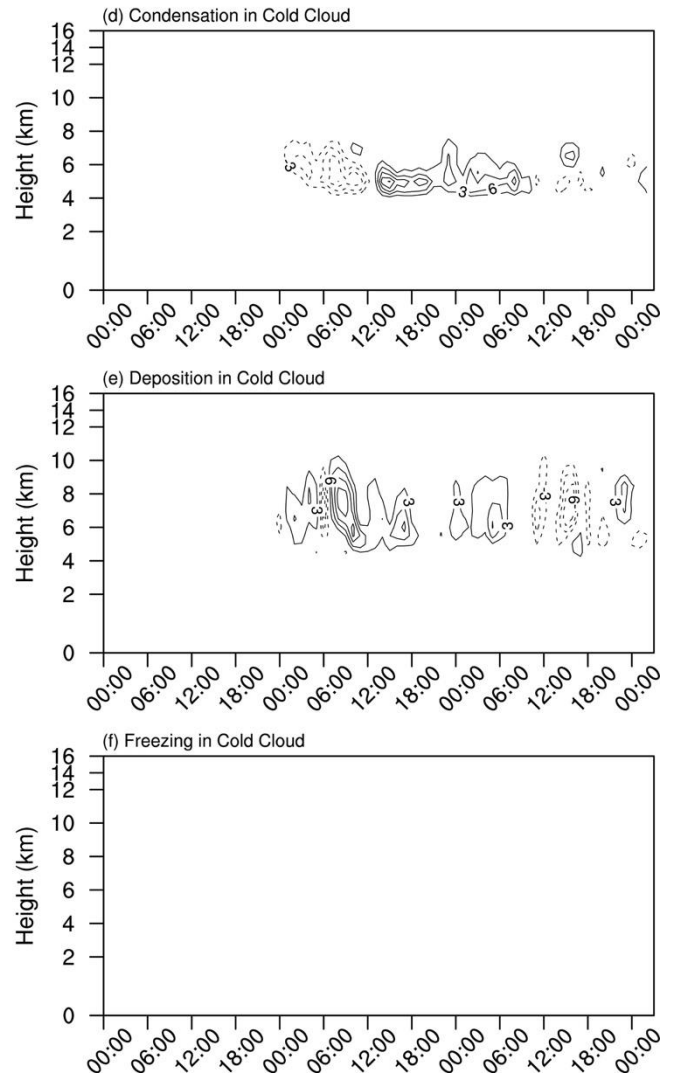
Figure S13. Differences with time (abscissa) and height (ordinate) in latent heat release (K d⁻¹) from (a) condensation, (b) deposition, and (c) freezing processes between D1 and CLEAN averaged over R1 for warm cloud. (d–f) Same as (a–c) but for cold cloud.
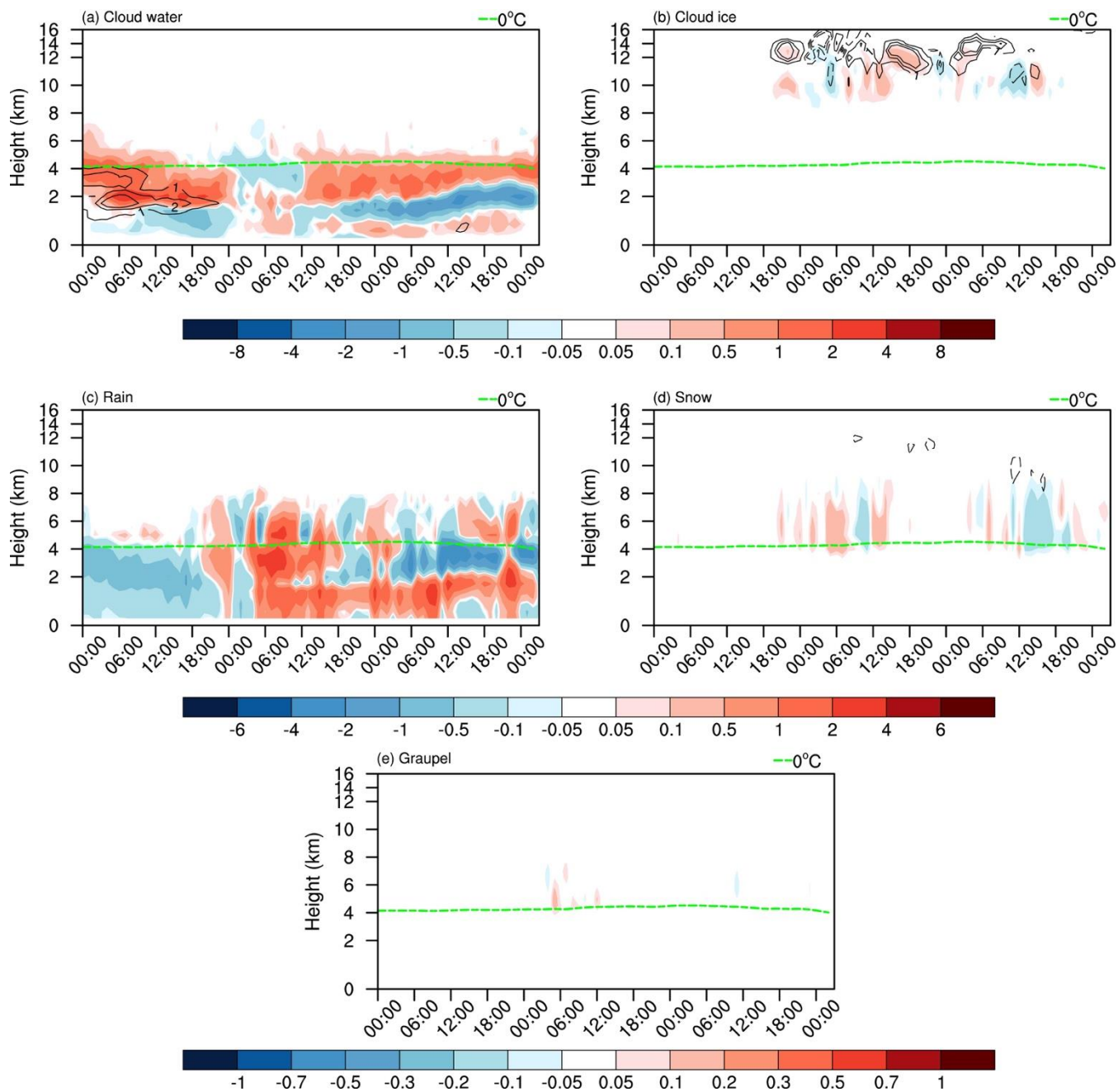
Figure S14. Differences with time (abscissa) and height (ordinate) in (a) cloud water (shading; 10^{-5} kg kg^{-1}) and CDNC (contour; 10^7 kg^{-1}), (b) cloud ice (shading; 10^{-5} kg kg^{-1}) and CINC (contour; 10^4 kg^{-1}), (c) rain (shading; unit: 10^{-5} kg kg^{-1}) and rain number concentration (contour; 10^5 kg^{-1}), (d) snow (shading; 10^{-4} kg kg^{-1}) and snow number concentrations (contour; 10^3 kg^{-1}), and (e) graupel (shading; 10^{-4} kg kg^{-1}) and graupel number concentration (contour; 10^3 kg^{-1}) between D2 and CLEAN averaged over R1.

10

Figure S15. Differences with time (abscissa) and height (ordinate) in latent heat release (K d^{-1}) from (a) condensation, (b) deposition, and (c) freezing processes between D2 and CLEAN averaged over R1 for 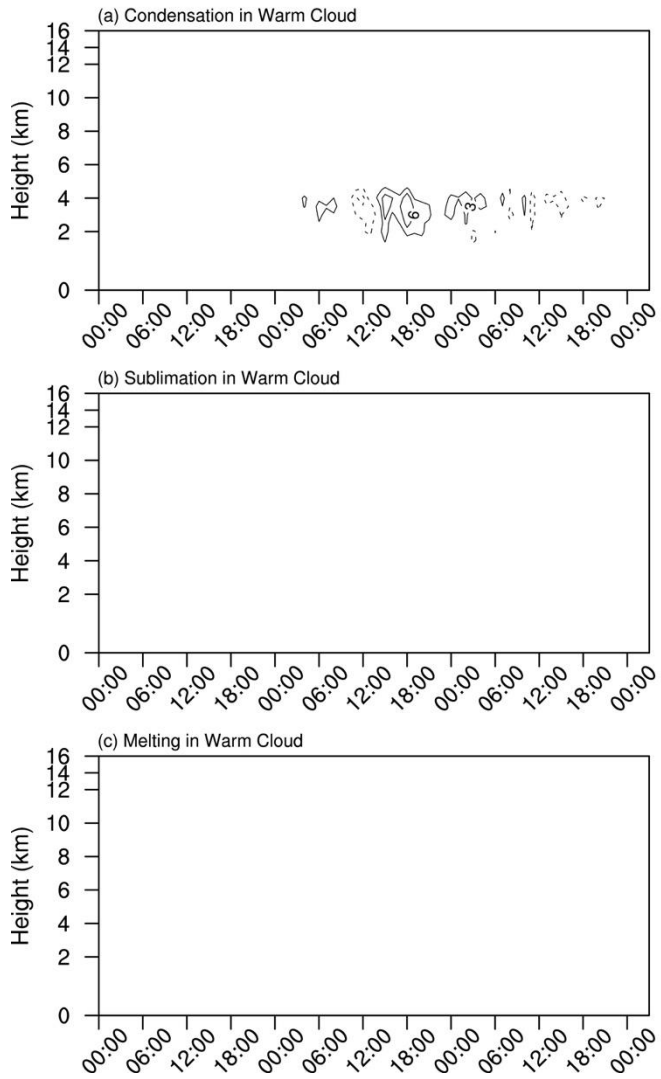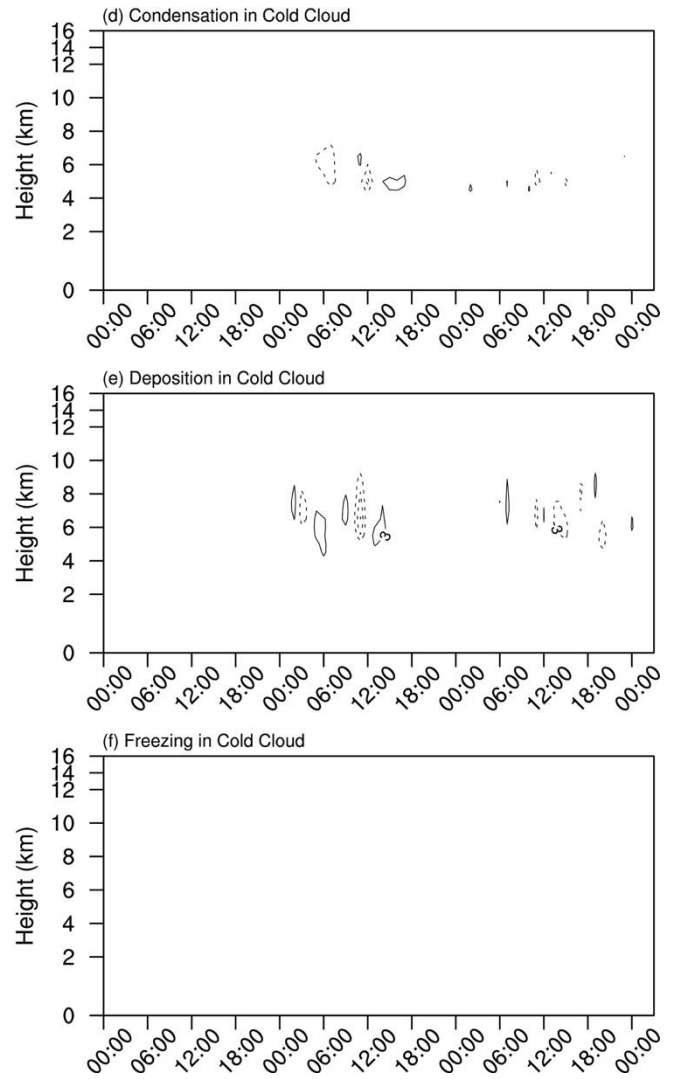warm cloud. (d–f) Same as (a–c) but for cold cloud. Zero-value contour lines are omitted, and negative values are dashed. The contour interval is 3 K d^{-1}.
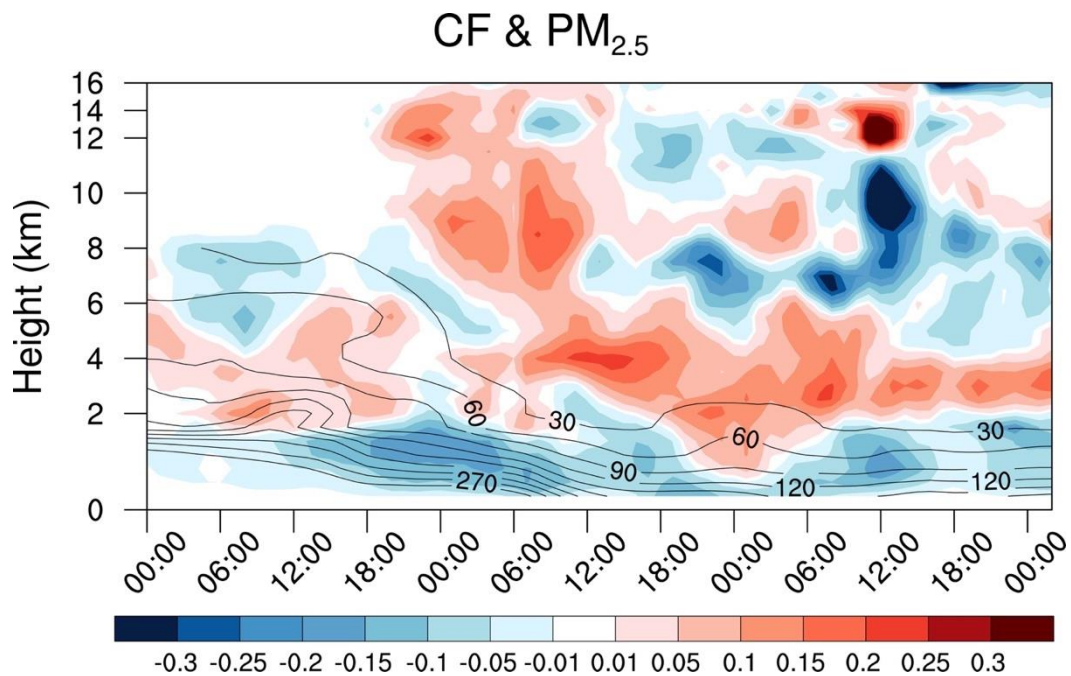
Figure S16. Differences in the time-height cross section of cloud factor CF (shading; unitless) and PM$_{2.5}$ concentration (contour; μg m^{-3}) averaged over R1 between 10× and CLEAN.

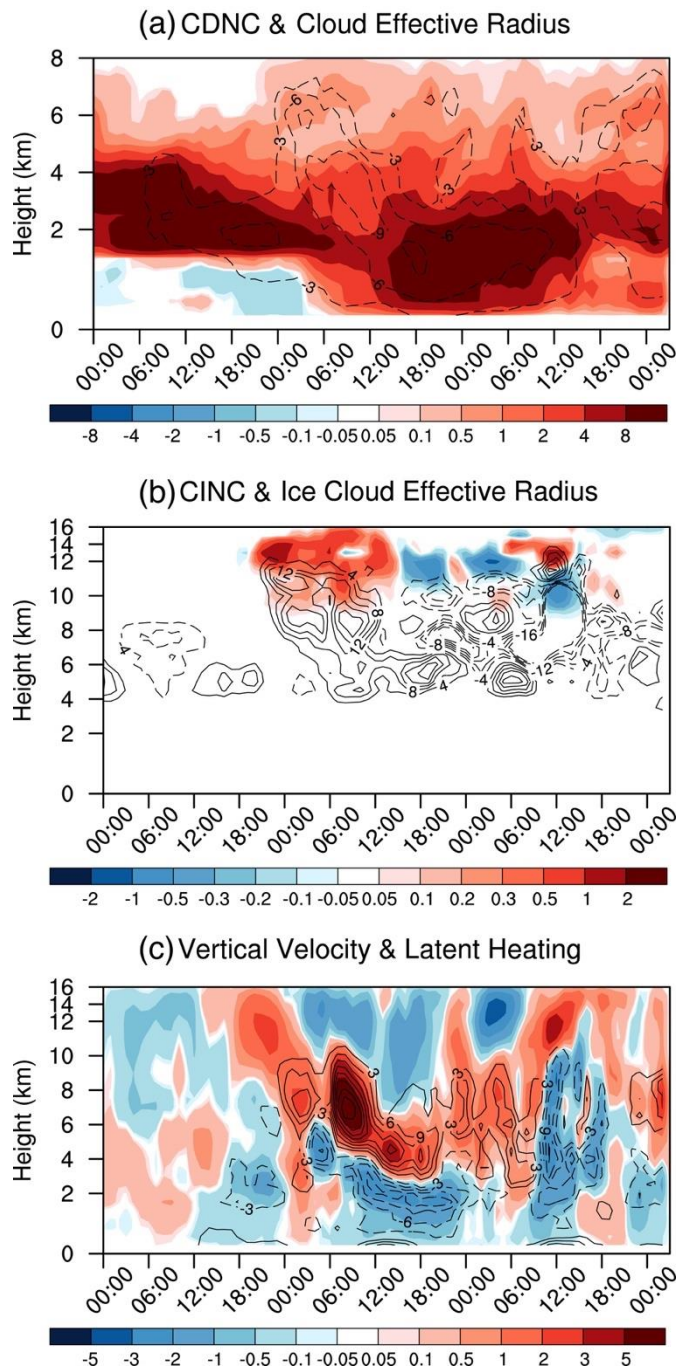**Figure S17. Differences with time (abscissa; from 00Z on December 14 to 02Z on December 17) and height (ordinate) in (a) CDNC (shading; 10^7 kg^{-1}) and cloud effective radius (μm), (b) CINC (shading; 10^5 kg^{-1}) and ice cloud effective radius (contour; μm), and (c) vertical velocity (shading; cm s^{-1}) and latent heating (contour; K d^{-1}) averaged over R1 between 10× and CLEAN.**
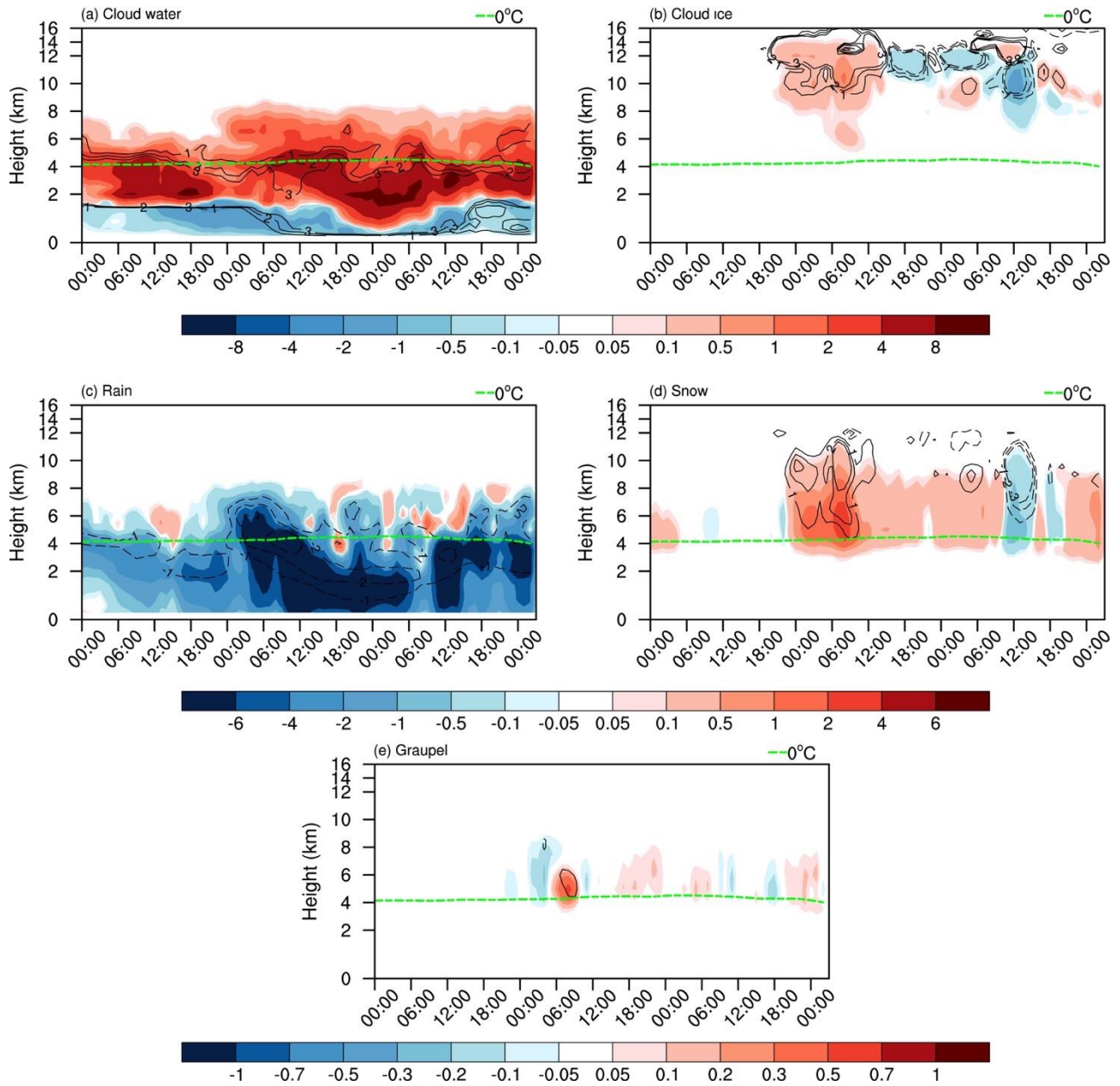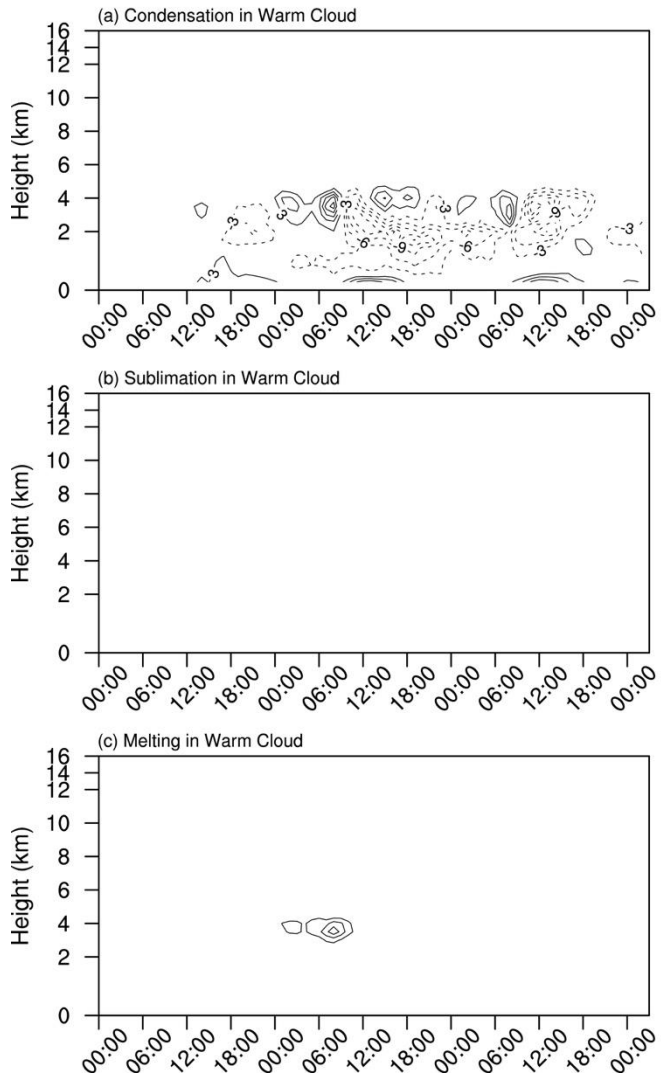
Figure S18. Differences with time (abscissa) and height (ordinate) in (a) cloud water (shading; 10^{-5} kg kg^{-1}) and CDNC (contour; 10^7 kg^{-1}), (b) cloud ice (shading; 10^{-5} kg kg^{-1}) and CINC (contour; 10^4 kg^{-1}), (c) rain (shading; 10^{-5} kg kg^{-1}) and rain number concentration (contour; 10^5 kg^{-1}), (d) snow (shading; 10^{-4} kg kg^{-1}) and snow number concentration (contour; 10^3 kg^{-1}), and (e) graupel (shading; 10^{-4} kg kg^{-1}) and graupel number concentration (contour; 10^3 kg^{-1}) between 10× and CLEAN averaged over R1.
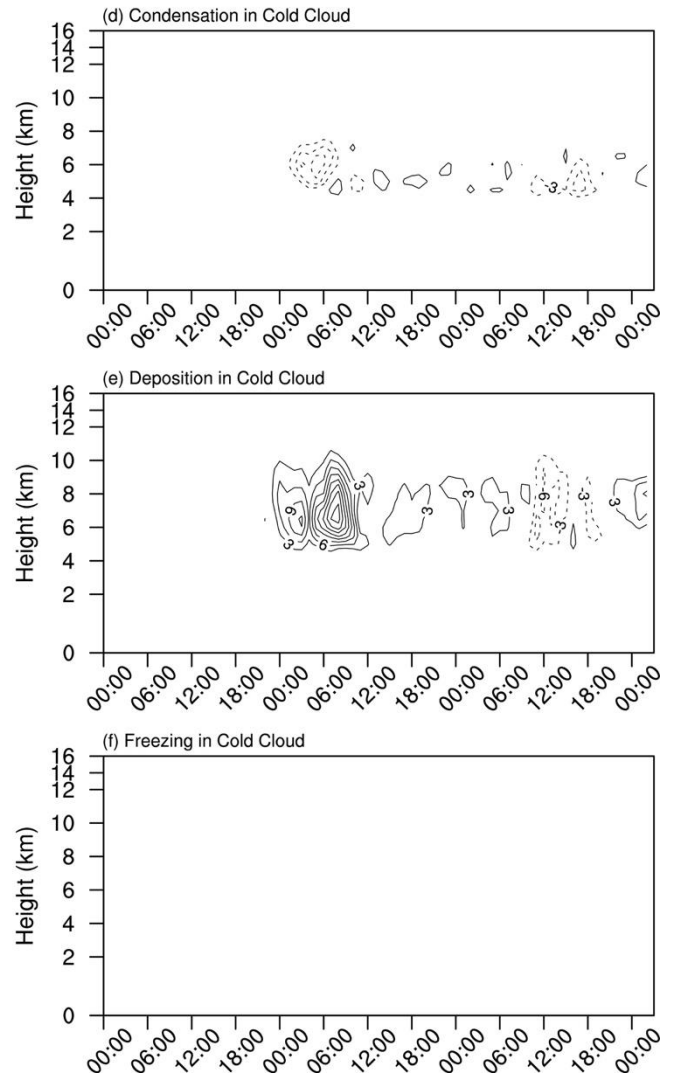
14

Figure S19. Differences with time (abscissa) and height (ordinate) in latent heat release (K d⁻¹) from (a) condensation, (b) deposition, and (c) freezing processes between 10× and CLEAN averaged over R1 for warm cloud. (d–f) Same as (a–c) but for cold cloud.
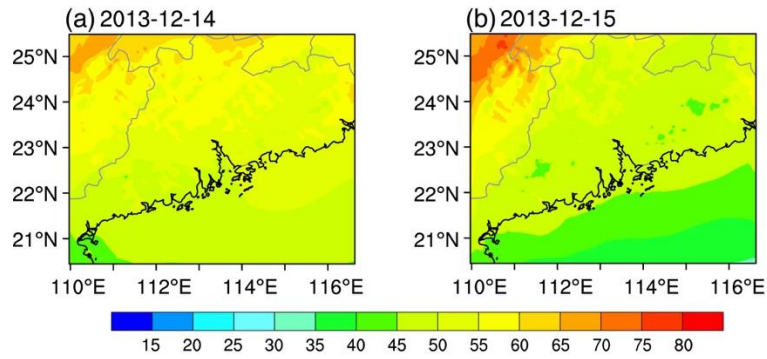
Figure S20. Spatial distribution of wind shear (m s⁻¹) on (a) December 14 and (b) December 15 in 2013 in the CTL run. Wind shear is calculated as differences between maximum wind speed and minimum wind speed at 0–10 km. Spatial distribution of column-integrated water vapor (shading; mm day⁻¹) and 925-hPa wind (vector; m s⁻¹) on (c) December 14 and (d) December 15 in 2013 in CTL.

Figure S21. Distribution with time (abscissa) and height (ordinate) in (a) cloud water (shading; 10^{-5} kg kg^{-1}) and CDNC (contour; unit: 10^7 kg^{-1}), (b) cloud ice (shading; 10^{-5} kg kg^{-1}) and CINC (contour; 10^4 kg^{-1}), (c) rain (shading; 10^{-5} kg kg^{-1}) and rain number concentration (contour; 10^5 kg^{-1}), (d) snow (shading; 10^{-4} kg kg^{-1}) and snow number concentrations (contour; 10^3 kg^{-1}), and (e) graupel (shading; 10^{-4} kg kg^{-1}) and graupel number concentration (contour; 10^3 kg^{-1}) averaged over R2 from CTL run.
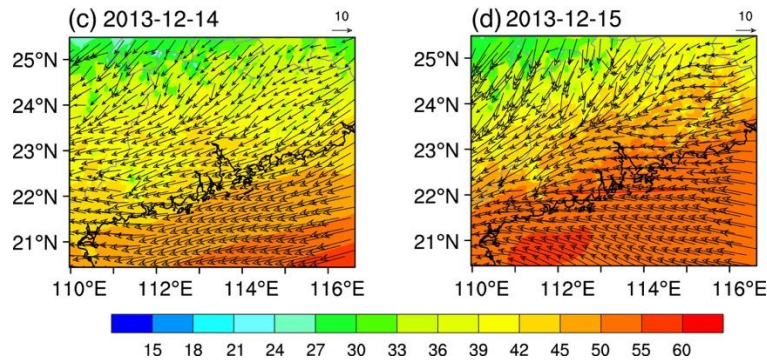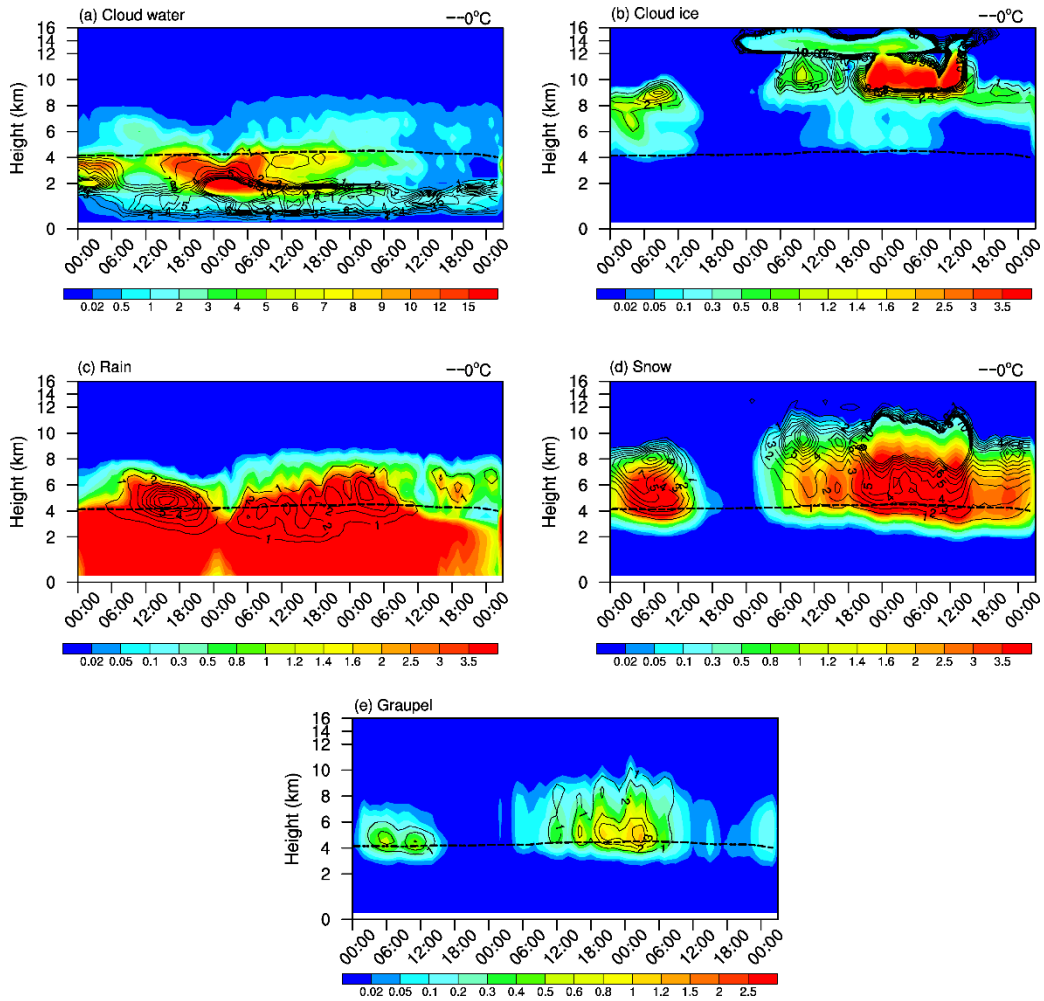
Figure S22. Differences with time (abscissa) and height (ordinate) in (a) cloud water (shading; 10^{-5} kg kg^{-1}) and CDNC (contour; 10^7 kg^{-1}), (b) cloud ice (shading; 10^{-5} kg kg^{-1}) and CINC (contour; 10^4 kg^{-1}), (c) rain (shading; 10^{-5} kg kg^{-1}) and rain number concentration (contour; 10^5 kg^{-1}), (d) snow (shading; 10^{-4} kg kg^{-1}) and snow number concentrations (contour; 10^3 kg^{-1}), and (e) graupel (shading; 10^{-4} kg kg^{-1}) and graupel number concentration (contour; 10^3 kg^{-1}) between CTL and CLEAN averaged over R2.

Figure S23. Differences with time (abscissa) and height (ordinate) in latent heat release (K d^{-1}) from (a) condensation, (b) deposition, and (c) freezing processes between CTL and CLEAN averaged over R2 for warm cloud. (d–f) Same as (a–c) but for cold cloud.
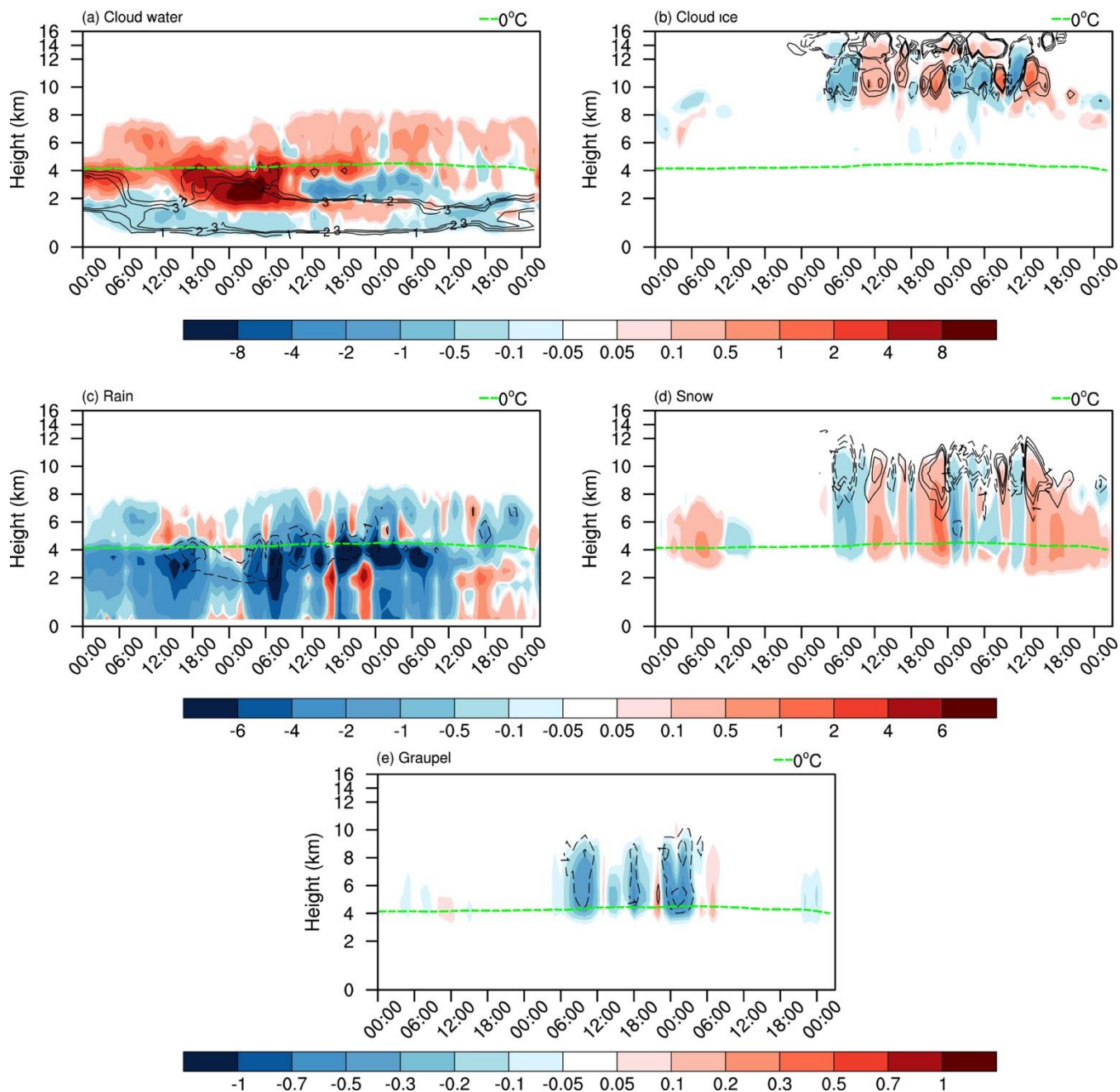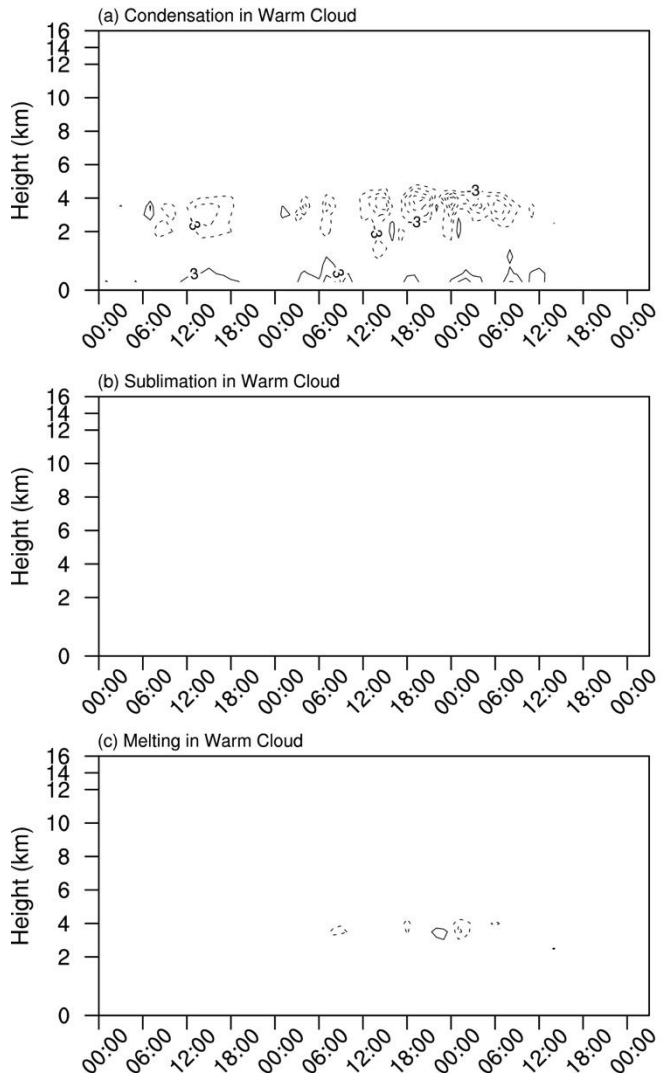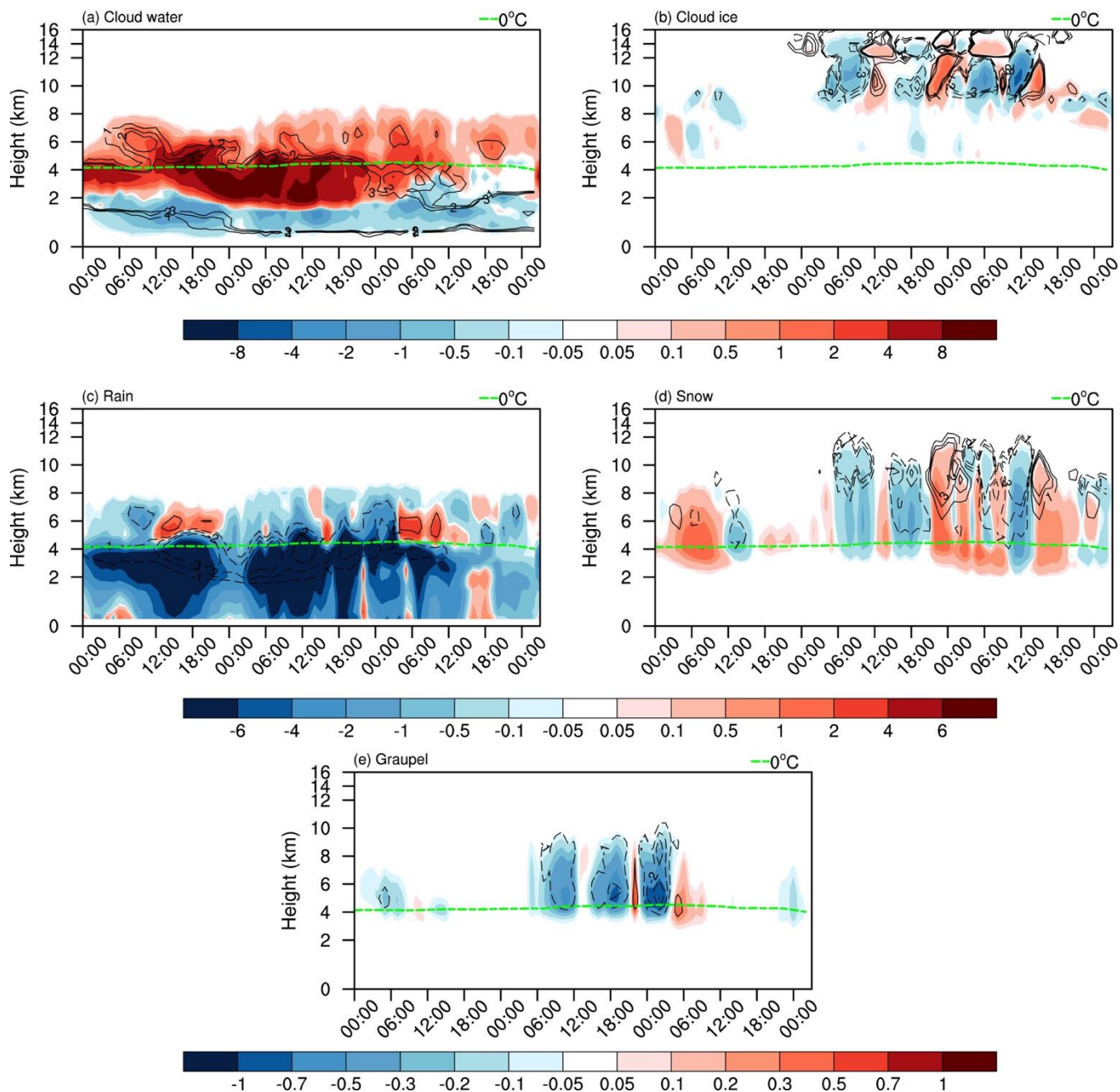
Figure S24. Differences with time (abscissa) and height (ordinate) in (a) cloud water (shading; 10^{-5} kg kg^{-1}) and CDNC (contour; 10^7 kg^{-1}), (b) cloud ice (shading; 10^{-5} kg kg^{-1}) and CINC (contour; 10^4 kg^{-1}), (c) rain (shading; 10^{-5} kg kg^{-1}) and rain number concentration (contour; 10^5 kg^{-1}), (d) snow (shading; 10^{-4} kg kg^{-1}) and snow number concentrations (contour; 10^3 kg^{-1}), and (e) graupel (shading; 10^{-4} kg kg^{-1}) and graupel number concentration (contour; 10^3 kg^{-1}) between 10× and CLEAN averaged over R2.
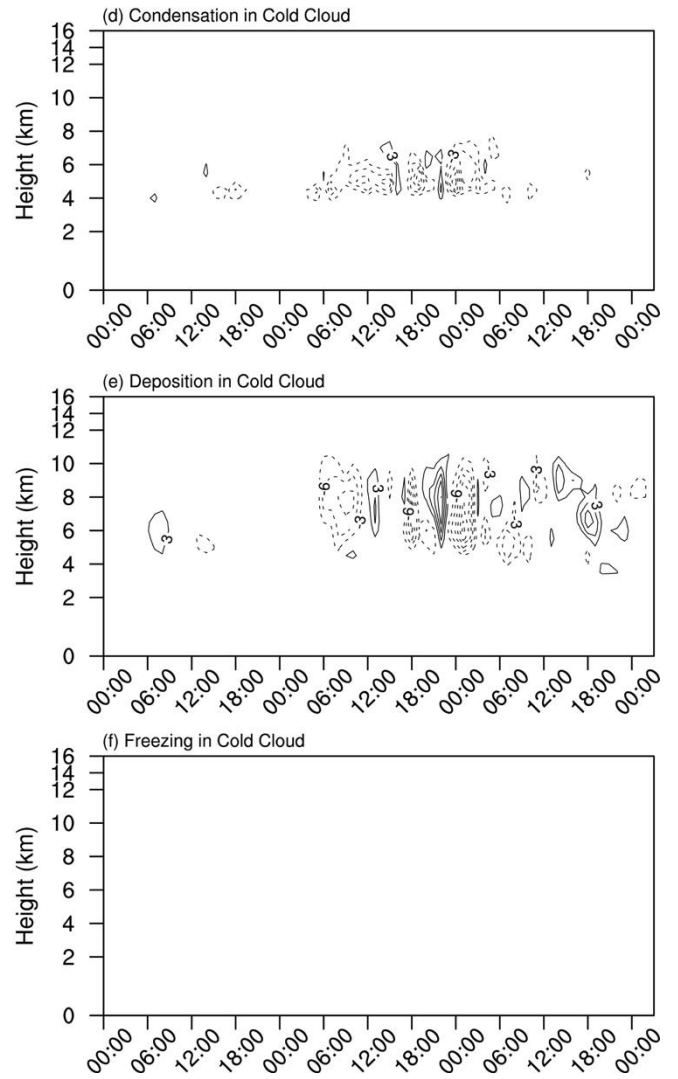
20

Figure S25. Differences with time (abscissa) and height (ordinate) in latent heat release (K d⁻¹) from (a) condensation, (b) deposition, and (c) freezing processes between 10× and CLEAN averaged over R2 for warm cloud. (d–f) Same as (a–c) but for cold cloud.
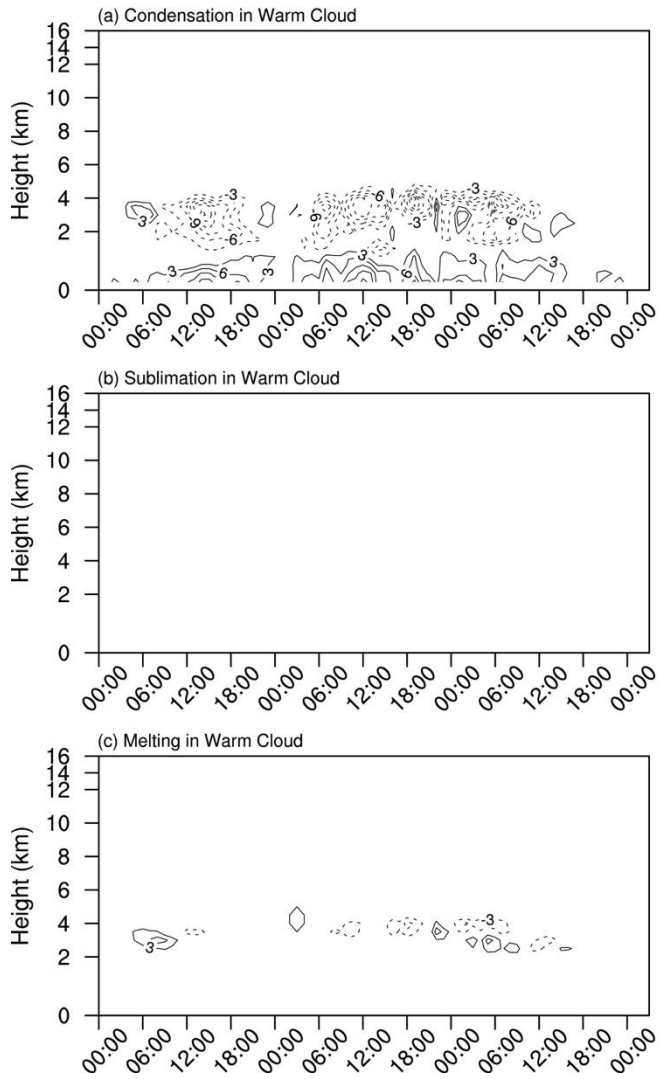
T2

(a) CTL-CLEAN

(b) D1-CLEAN

Column Water Vapor

(c) CTL-CLEAN

(d) D1-CLEAN
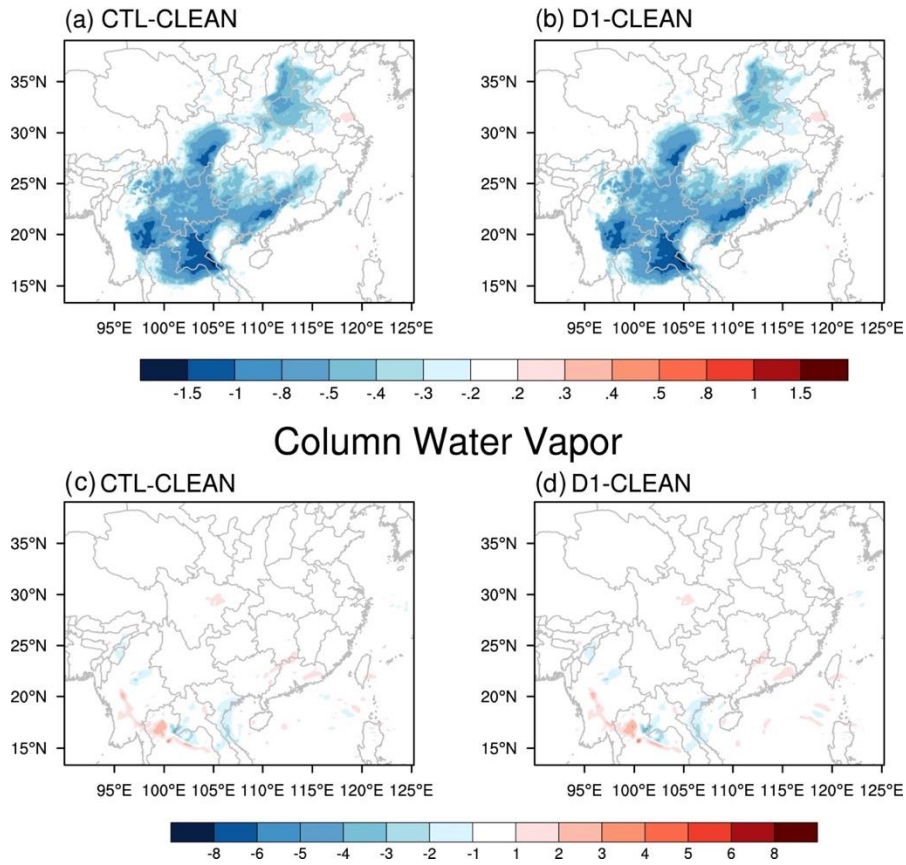
Figure S26. Differences in 2-m temperature (K) between (a) CTL and CLEAN and (b) D1 and CLEAN on December 15. (c, d) Same as (a, b) but for column water vapor (mm).

Precipitation

(a) CTL-CLEAN

(b) D1-CLEAN

Figure S27. Differences in precipitation (mm) between (a) CTL and CLEAN and (b) D1 and CLEAN on December 15 based on domain 1 output.

References

Binkowski, F. S. and Shankar, U.: The regional particulate matter model: 1. Model description and preliminary results, J. Geophys. Res., 100(D12), 26191, doi:10.1029/95JD02093, 1995.

Chapman, E. G., Gustafson, W. I., Easter, R. C., Barnard, J. C., Ghan, S. J., Pekour, M. S. and Fast, J. D.: Coupling aerosol-cloud-radia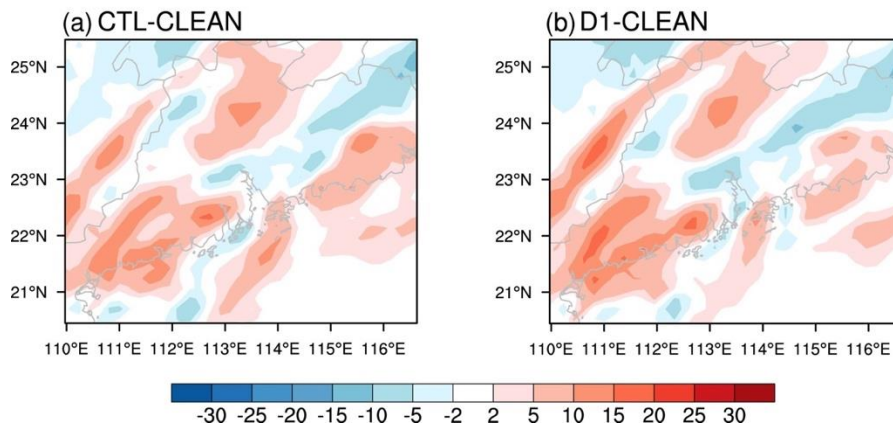tive processes in the WRF-Chem model: Investigating the radiative impact of elevated point sources, Atmos. Chem. Phys., 9(3), 945–964, doi:10.5194/acp-9-945-2009, 2009.

Chen, F. and Dudhia, J.: Coupling an advanced land surface–hydrology model with the Penn State–NCAR MM5 modeling system. Part I: Model implementation and sensitivity, Mon. Weather Rev., 129(4), 569–585, doi:10.1175/1520-0493(2001)129<0569:CAALSH>2.0.CO;2, 2001.

Easter, R. C., Ghan, S. J., Zhang, Y., Saylor, R. D., Chapman, E. G., Laulainen, N. S., Abdul-Razzak, H., Leung, L. R., Bian, X. and Zaveri, R. A.: MIRAGE: Model description and evaluation of aerosols and trace gases, J. Geophys. Res. D Atmos., 109(20), doi:10.1029/2004JD004571, 2004.

Fast, J. D., Gustafson, W. I., Easter, R. C., Zaveri, R. A., Barnard, J. C., Chapman, E. G., Grell, G. A. and Peckham, S. E.: Evolution of ozone, particulates, and aerosol direct radiative forcing in the vicinity of Houston using a fully coupled meteorology-chemistry-aerosol model, J. Geophys. Res. Atmos., 111(21), 1–29, doi:10.1029/2005JD006721, 2006.

Hong, S.-Y., Noh, Y. and Dudhia, J.: A new vertical diffusion package with an explicit treatment of entrainment processes., Mon. Weather Rev., 134(9), 2318–2341, doi:10.1175/MWR3199.1, 2006.

Iacono, M. J., Delamere, J. S., Mlawer, E. J., Shephard, M. W., Clough, S. A. and Collins, W. D.: Radiative forcing by long-lived greenhouse gases: Calculations with the AER radiative transfer models, , 113, 2–9, doi:10.1029/2008JD009944, 2008.

Kain, J. S. and J. M. Fritsch: A one-dimensional entraining/detraining plume model and its application in convective parameterization, J. Atmos. Sci., 47, 2784–2802, doi.org/10.1175/1520-0469(1990)047<2784:AODEPM>2.0.CO;2, 1990.

Morrison, H., Thompson, G. and Tatarskii, V.: Impact of cloud microphysics on the development of trailing stratiform precipitation in a simulated squall line: Comparison of one- and two-moment schemes, Mon. Weather Rev., 137(3), 991–1007, doi:10.1175/2008MWR2556.1, 2009.

Skamarock, W. C., Klemp, J. B., Dudhia, J., Gill, D. O., Barker, D. M., Duda, M. G., Huang, X.-Y., Wang, W. and Powers, J. G.: A description of the advanced research WRF version 3. [online] Available from: https://pdfs.semanticscholar.org/ace5/4d4d1d6c9914997ad8f4e410044fdeb95b9d.pdf (Accessed 15 May 2018), 2008.

Yang, Q., Gustafson, W. I., Fast, J. D., Wang, H., Easter, R. C., Morrison, H., Lee, Y. N., Chapman, E. G., Spak, S. N. and Mena-Carrasco, M. A.: Assessing regional scale predictions of aerosols, marine stratocumulus, and their interactions during VOCALS-REx using WRF-Chem, Atmos. Chem. Phys., 11(23), 11951–11975, doi:10.5194/acp-11-11951-2011, 2011.

Zaveri, R. A. and Peters, L. K.: A new lumped structure photochemical mechanism for large-scale applications, J. Geophys.

Res. Atmos., 104(D23), 30387–30415, doi:10.1029/1999JD900876, 1999.

Zaveri, R. A., Easter, R. C., Fast, J. D. and Peters, L. K.: Model for simulating aerosol interactions and chemistry (MOSAIC), J. Geophys. Res. Atmos., 113(13), doi:10.1029/2007JD008782, 2008.

Zhao, C., Wang, Y., Choi, Y. and Zeng, T.: Summertime impact of convective transport and lightning NOx production over North America: Modeling dependence on meteorological simulations, Atmos. Chem. Phys., 9(13), 4315–4327, doi:10.5194/acp-9-4315-2009, 2009.

Zhao, C., Liu, X., Leung, L. R., Johnson, B., Mcfarlane, S. A., Jr, W. I. G., Fast, J. D. and Easter, R.: The spatial distribution of mineral dust and its shortwave radiative forcing over North Africa: modeling sensitivities to dust emissions and aerosol size treatments, Atmos. Chem. Phys., 10, 8821–8838, doi:10.5194/acp-10-8821-2010, 2010.

Zhao, C., Liu, X., Leung, L. R. and Hagos, S.: and Physics Radiative impact of mineral dust on monsoon precipitation variability over West Africa, (2007), 1879–1893, doi:10.5194/acp-11-1879-2011, 2011.

Zhao, C., Chen, S., Leung, L. R., Qian, Y., Kok, J. F., Zaveri, R. A. and Huang, J.: Uncertainty in modeling dust mass balance and radiative forcing from size parameterization, Atmos. Chem. Phys., 13(21), 10733–10753, doi:10.5194/acp-13-10733-2013, 2013.